

UNIVERSITY OF BIRMINGHAM

Research at Birmingham

Natural gas potential of Carboniferous and Permian transitional shales in central Hunan, South China

Zhao, Zhenghui; Tan, Jianqiang ; Ju, Yiwen; Hilton, Jason; Yang, Rongfeng; Zhou, Ping; Huang, Yanran; Ning, Bowen; Liu, Jisong

DOI:

[10.1016/j.jngse.2018.05.024](https://doi.org/10.1016/j.jngse.2018.05.024)

License:

Creative Commons: Attribution-NonCommercial-NoDerivs (CC BY-NC-ND)

Document Version

Peer reviewed version

Citation for published version (Harvard):

Zhao, Z, Tan, J, Ju, Y, Hilton, J, Yang, R, Zhou, P, Huang, Y, Ning, B & Liu, J 2018, 'Natural gas potential of Carboniferous and Permian transitional shales in central Hunan, South China' *Journal of Natural Gas Science and Engineering*, vol. 55, pp. 520-533. <https://doi.org/10.1016/j.jngse.2018.05.024>

[Link to publication on Research at Birmingham portal](#)

Publisher Rights Statement:

Checked for eligibility: 24/05/2018
<https://doi.org/10.1016/j.jngse.2018.05.024>

General rights

Unless a licence is specified above, all rights (including copyright and moral rights) in this document are retained by the authors and/or the copyright holders. The express permission of the copyright holder must be obtained for any use of this material other than for purposes permitted by law.

- Users may freely distribute the URL that is used to identify this publication.
- Users may download and/or print one copy of the publication from the University of Birmingham research portal for the purpose of private study or non-commercial research.
- User may use extracts from the document in line with the concept of 'fair dealing' under the Copyright, Designs and Patents Act 1988 (?)
- Users may not further distribute the material nor use it for the purposes of commercial gain.

Where a licence is displayed above, please note the terms and conditions of the licence govern your use of this document.

When citing, please reference the published version.

Take down policy

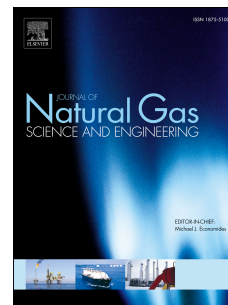
While the University of Birmingham exercises care and attention in making items available there are rare occasions when an item has been uploaded in error or has been deemed to be commercially or otherwise sensitive.

If you believe that this is the case for this document, please contact UBIRA@lists.bham.ac.uk providing details and we will remove access to the work immediately and investigate.

Accepted Manuscript

Natural gas potential of Carboniferous and Permian transitional shales in central Hunan, South China

Zhenghui Xiao, Jingqiang Tan, Yiwen Ju, Jason Hilton, Rongfeng Yang, Ping Zhou, Yanran Huang, Bowen Ning, Jisong Liu



PII: S1875-5100(18)30224-5

DOI: [10.1016/j.jngse.2018.05.024](https://doi.org/10.1016/j.jngse.2018.05.024)

Reference: JNGSE 2582

To appear in: *Journal of Natural Gas Science and Engineering*

Received Date: 29 July 2017

Revised Date: 22 April 2018

Accepted Date: 16 May 2018

Please cite this article as: Xiao, Z., Tan, J., Ju, Y., Hilton, J., Yang, R., Zhou, P., Huang, Y., Ning, B., Liu, J., Natural gas potential of Carboniferous and Permian transitional shales in central Hunan, South China, *Journal of Natural Gas Science & Engineering* (2018), doi: 10.1016/j.jngse.2018.05.024.

This is a PDF file of an unedited manuscript that has been accepted for publication. As a service to our customers we are providing this early version of the manuscript. The manuscript will undergo copyediting, typesetting, and review of the resulting proof before it is published in its final form. Please note that during the production process errors may be discovered which could affect the content, and all legal disclaimers that apply to the journal pertain.

1 Natural gas potential of Carboniferous and Permian transitional 2 shales in central Hunan, South China

3 Zhenghui Xiao^a, Jingqiang Tan^{b,*}, Yiwen Ju^c, Jason Hilton^d, Rongfeng Yang^a, Ping Zhou^e,
4 Yanran Huang^a, Bowen Ning^f, Jisong Liu^a

5
6 ^a Hunan Key Laboratory of Shale Gas Resource Utilization, School of Resource, Environment and Safety
7 Engineering, Hunan University of Science and Technology, Xiangtan 411201, Hunan, China

8 ^b Key Laboratory of Metallogenic Prediction of Nonferrous Metals and Geological Environment Monitoring,
9 Ministry of Education, School of Geosciences and Info-Physics, Central South University, Changsha 410083,
10 China

11 ^c College of Earth Sciences, University of Chinese Academy of Sciences, Beijing 100049, China

12 ^d School of Geography, Earth and Environmental Science, University of Birmingham, Edgbaston, Birmingham,
13 B15 2TT, UK

14 ^e School of Economics, Hunan Institute of Engineering, Xiangtan 411104, Hunan, China

15 ^f Henan Geological Exploration Institute of China Chemical Geology and Mine Bureau, Zhengzhou 450011,
16 Henan, China

17 * Corresponding authors: tanjingqiang@aliyun.com

19 Abstract

20 The Carboniferous Ceshui formation and Permian Longtan and Dalong formations
21 were deposited in transitional settings preserved in what is now central Hunan Province,
22 South China, as they are potential natural gas plays. In this study, we analysed the total
23 organic carbon (TOC), vitrinite reflectance (Ro), kerogen type, mineralogy, porosity,
24 permeability, and methane adsorption of representative shale samples from these rock units.
25 Our results indicate that TOC content can be as high as 9.2%, with a mean (\bar{x}) of 3.5%. The
26 Permian shale formations were deposited in more strongly reducing environments than the

27 Carboniferous Ceshui shale. The kerogen composition of the Carboniferous Ceshui shale is
28 dominated by Type III, while both of the Permian shales contain primarily Type II kerogens;
29 Ro values range from 1.1% to 2.4% (\bar{x} =1.6%). The organic matter in all the studied shales is
30 in the wet gas window of thermal maturity and is relatively less mature than Lower
31 Palaeozoic marine shales in south China. Mineral compositions are dominated by quartz
32 (\bar{x} =53.8%) and clay (\bar{x} =35.6%), suggesting a high brittleness index. Porosity ranges from
33 0.5% to 14% (\bar{x} =6.4%), while permeability varies from 0.0026 micro Darcy (mD) to 0.0640
34 mD (\bar{x} =0.0130 mD). The gas adsorption capacity varies from 1.24 to 4.53 cm³/g (\bar{x} =2.40
35 cm³/g). Relatively less mature shale samples (Ro<1.5%) have low methane adsorption
36 capacities, regardless of their TOC values. However, the methane adsorption capacity of
37 more mature (Ro>1.5%) shales samples exhibit a positive correlation with TOC content.

38 **Keywords:** Lower Carboniferous; Upper Permian; Natural gas; Transitional shale;
39 Unconventional reservoir; Hunan Province.

41 1. Introduction

42 The remarkable success of shale gas development in North America has triggered a
43 flourishing of shale gas exploration and increased the number of investigations into the gas
44 potential of shales worldwide (e.g., Bowker, 2007; Jarvie et al., 2007; Tang et al., 2014; Tan
45 et al., 2015). To enhance domestic energy supply via shale gas exploitation, the Chinese
46 government has already set ambitious plans. Geological surveys and exploration activities are
47 underway across the country (Tan et al., 2013). To date, China has begun developing several
48 shale gas fields in the Sichuan Basin (e.g., the Fuling, Weiyuan, and Changning shale gas
49 blocks).

50 In China, three types of organic rich shale are widely distributed in sedimentary
51 basins, comprising marine shales, marine-lacustrine transitional shales (hereafter referred to

52 as “transitional shales”), and lacustrine shales (Bu et al., 2015; Tan et al., 2015). Marine
53 shales in the Cambrian and Silurian strata and transitional shales in the Carboniferous and
54 Permian strata are widely distributed across South China (e.g. Tan et al., 2015; Zou et al.,
55 2010). Although natural gas has been successfully produced from the marine shales,
56 transitional shales have not been yet successfully developed (Dong et al., 2016). In the central
57 part of Hunan, Carboniferous and Permian transitional shales occur in thick and laterally
58 extensive beds (Bao et al., 2016; Gu et al., 2015; Jing et al., 2013; Xu et al., 2015). Previous
59 studies have shown that Carboniferous and Permian paralic coal-bearing strata constitute
60 source rocks for conventional petroleum fields in this region (Wang et al., 2010; Zhan et al.,
61 2006; Zhou et al., 2014; Zhu et al., 2012). These transitional shales have been more recently
62 identified as promising targets of shale gas exploration (Bao et al., 2016; Gu et al., 2015;
63 Liang et al., 2014; Luo et al., 2012). National petroleum companies, including Sinopec, have
64 already shown strong interest in developing natural gas resources from transitional shale
65 intervals. Therefore, there is an urgent need to characterise these shale intervals and evaluate
66 their reservoir potential.

67 It has been recognized that no two shale gas systems are exactly alike, and thus
68 exploitation strategies differ from one system to the next (Tan, et al., 2015). However,
69 prolific shale plays are commonly distinguished using certain minimal technical thresholds.
70 These include, but are not limited to: shale lateral extent and effective thickness, organic
71 matter richness, thermal maturity, mineralogy, porosity, permeability, adsorptive capacity,
72 and gas-in-place (GIP) (Bowker, 2007; Jarvie et al., 2007; Tan, et al., 2013; 2015). These
73 indices have been widely applied to evaluate the reservoir potential of marine shales in South
74 China. However, for transitional shales, numerous issues remain concerning the composition
75 and source(s) of organic material, depositional environment, thermal maturity, petrophysical
76 properties, and methane adsorption capacity. Additionally, the correlations among organic

77 materials, mineralogy, and depositional conditions, as well as the influences of porosity and
78 permeability, and the relative effects of total organic carbon (TOC) and thermal maturity on
79 methane adsorption have not been clarified. This study aims to investigate these problems
80 through a systematic characterization of transitional shales from the Carboniferous Ceshui
81 formation and the Permian Longtan and Dalong formations in the central region of Hunan.
82 We comprehensively analysed the TOC content, organic matter type, thermal maturity,
83 mineral composition, reservoir physical properties, and gas adsorption capacity of the shales.
84 We then compared our results with those reported for prolific shale plays in China and the
85 United States. Lastly, we discuss the correlations among the selected reservoir
86 characterisation parameters.

87

88 **2. Materials and Methods**

89 *2.1 Geological setting and shale deposition in central Hunan*

90 The study area is located in the Middle Yangtze Region and in the north of the South
91 China fold system (Fig. 1a). It lies east of the Hengshan Uplift, and west of the Xuefeng
92 Uplift. This region is tectonically composed of five subunits. From north to south they are the
93 Lianyuan Depression, Longshan Uplift, Shaoyang Depression, Guandimiao Uplift, and the
94 Lingling Depression (Fig. 1b). Regional faults extend primarily in the NE-NNE direction,
95 and include the Chengbu-Xinhua fault, Qiyang Arc fault, Miluo-Shaoyang fault, Xinshao-
96 Xinning fault, and Zhuzhou-Shuangpai fault (Fig. 2). Additionally, thrust nappe and gravity
97 gliding structures have been formed by multiple tectonic events. The Lianyuan and Shaoyang
98 depression began forming during the Ordovician at the onset of the Caledonian orogeny. The
99 Qiyang arc was dominantly formed through structural deformation caused by the Triassic
100 Indosinian orogeny (Li, et al., 2013; Wang et al., 2010).

101 Shales are well developed in certain formations of the study area. Sedimentary strata
102 are characterized by carbonates interbedded with clastics deposited in the Late Palaeozoic to
103 Middle Triassic. The region has experienced four primary sedimentary cycles from the
104 Devonian to the Permian (Jing et al., 2013; Xu et al., 2015). The first sedimentary cycle
105 occurred between the Tiaomajian and Qiziqiao periods during the Devonian when a
106 transgression initiated during a large-scale geological extension and was followed by a
107 regression generated by the Liujiang orogeny. This cycle resulted in the deposition of the
108 Shetianqiao and Qiziqiao marine shales. The second transgression started in the Mississippian
109 (early Carboniferous), but ended as a full-scale regression in the mid-Mississippian with the
110 deposition of the Ceshui formation as transitional beds formed under the
111 alternating influences of shallow marine and shoreline environments (Fig. 1c) (Shao et al.,
112 1992). The third cycle was primarily controlled by the Dongwu tectonic movement and is the
113 largest transgression that occurred during the development of the mid- to late Carboniferous
114 paraplatform. However, this transgression was terminated by a full-scale regression during
115 the early Lopingian (late Permian) (Fig. 1c), and coastal marsh shales were subsequently
116 deposited (Gu et al., 2015; Ji et al., 2011). The fourth cycle persisted for a shorter time (i.e.,
117 only during the Lopingian), and resulted in the deposition of the Dalong formation (Fig. 1c).
118 During this time, siliciclastic rocks, siliceous limestone, and shales were deposited in littoral-
119 bathyal-abyssal facies (Fig. 1c) (Feng et al., 1993).

120 2.2 Samples

121 Fresh transitional shale samples are exposed in some outcrops of the study area. A
122 total of 96 representative samples were collected from the Shimingqiao (SMQ), Qixingjie
123 (QXJ), Duanpoqiao (DPQ), Tantou (TT), Doulishan (DLS), Nantang (NT), Jilong (JL),
124 Jingzhushan (JZS), Zhaoyang (ZY), Liangshuijing (LSJ), Xiandong (XD), Lumaojiang

125 (LMJ), and Douling (DL) sections (Fig. 1b). Generally, shale samples were collected from at
126 least 1 m deep, and every 10 m from the bottom to top of the exposed sections.

127 *2.3 Methods*

128 The selected samples were analysed for TOC, vitrinite reflectance (R_o), kerogen type,
129 mineralogy, porosity, permeability, and methane adsorption.

130 TOC contents were measured using a Leco carbon-sulphur analyser and reported as
131 the weight percentage (wt%) of the total rock material. Samples were crushed into a powder
132 <200 mesh, and 1-2 g samples were pyrolysed to 600°C. Thin-sections of 42 samples were
133 prepared for investigation mineral components and structural fabrics. The samples were
134 examined using a Zeiss Axiophot Electronic Microscope equipped with a Carl Zeiss Axiocam
135 digital camera and Axiovision 2.0 software. This system was capable of taking high-
136 resolution photomicrographs under magnification of 10x, 20x, 30x, 40x, and 50x. Kerogen
137 type was analysed by transmitted light microscopy. Thermal maturity, represented by R_o ,
138 was determined using a MVP-3 microscope photomultiplier.

139 A total of 25 samples were analysed with a D/max-2600 X-ray diffractometer (XRD)
140 to quantify the principal mineralogical constituents. The diffraction data were recorded from
141 4° to 75° 2θ with a step width of 0.02° , and a counting time of 4 s per step. Experimental
142 conditions were set to 40 kV and 30 mA. The measured data were analysed qualitatively
143 using EVA (Bruker) software, and quantitatively using AutoQuant software.

144 High-resolution scanning electron microscopy (SEM) analysis was performed on
145 representative samples with different TOC contents and lithological types. Small subsamples
146 0.3-0.5 cm thick, 0.5-1.0 cm wide, and >2 cm long were cut and prepared. The subsamples
147 were dried in an oven at 40°C for 24 h to remove moisture. Analysis was conducted using a
148 TESCAN VEGA scanning probe microscope, and images were obtained under high vacuum
149 at 20 kV acceleration voltage.

150 Porosity was measured with an ULTRAPORE-200A helium porosimetre.
151 Permeability was tested using an ULTRA-PERMTM200 permeametre. Measurements were
152 performed at room temperature and normal pressure (~23°C, 102 kPa) and 50% humidity.

153 Methane adsorption isotherms were measured for selected moisture-equilibrated
154 samples at 40°C. The experimental procedure was: 1) de-gas the sample, 2) conduct leak
155 tests, 3) determine the void volume as well as the sample volume using helium expansion, 4)
156 evacuate for 60 min at 1 MPa to remove helium, and 5) perform the methane adsorption
157 measurement (Tan, et al., 2014a). The Langmuir isotherm was applied to model gas
158 adsorption capacity. The equation used is: $V = V_L P / (P_L + P)$ (Pan, et al., 2015, and references
159 therein), where V is the volume of absorbed gas, V_L is the Langmuir volume (on the basis of
160 monolayer adsorption), which is the maximum adsorption capacity of the absorbent, P is the
161 gas pressure, and P_L is the Langmuir pressure, at which the absorbed gas content (V) is equal
162 to half of the Langmuir volume (i.e., $0.5 V_L$).

163

164 **3. Results**

165 *3.1 Organic geochemical characterization*

166 The TOC content of the 96 shale samples ranges from 0.4% to 9.2% (Table 1), with a
167 mean value of 3.5%. Most of sections exhibit mean TOC contents >2%, indicating that these
168 Carboniferous-Permian transitional shales are typically organic-rich. As shown in Tables 1
169 and 2, the TOC content of samples from different sections varies significantly. In general, the
170 TOC content decreases from the Longtan shale to the Dalong shale, and again in the Ceshui
171 shale.

172 Organics of the shales from the Carboniferous Ceshui formation are principally
173 composed of vitrinite (i.e., euvitrinite and vitrodetrinite). This suggests that the organic
174 matter is more derived from higher plants, and the organic matter constituents are

175 characteristic of type III kerogen (Definition can be seen in Appendix 1). In contrast, the
176 kerogen type of the shales from the Permian Longtan and Dalong formations are dominated
177 by exinite (i.e., abundant humic amorphous bodies and a small number of sporopollen bodies).
178 The vitrinite (i.e. euvitrinite and vitrodetrinite) content is less than 30%. This implies that the
179 organics of the Upper Permian shales are primarily type II kerogen (Definition can be seen in
180 Appendix 2).

181 Ro values range from 1.1% to 2.4% ($\bar{x}=1.6\%$) (Tables 1 and 2). This suggests that the
182 Carboniferous-Permian transitional shales have entered into a stage of high maturation.
183 Organic matter is located in the late wet gas and dry gas window of thermal maturity.
184 Comparatively, Ro values are high in the Ceshui shale, and gradually reduce from these
185 samples to the Longtan shale, and finally the Dalong shale, reflecting a burial depth control
186 on thermal maturity.

187 3.2 Mineralogy and lithology

188 3.2.1 Mineralogy

189 The XRD mineralogical data are shown in Table 2. Major constituents are quartz and
190 clay minerals. Minor mineral components include calcite, feldspar, and pyrite. The quartz
191 content ranges between 39.0% and 86.2% ($\bar{x}=53.8\%$) and clay minerals range from 11.0% to
192 69.1% ($\bar{x}=35.6\%$). Interestingly, the total amount of brittle minerals (i.e., quartz, feldspar,
193 calcite, and dolomite) is >60% (Table 2), indicating that the condition of the shale is likely
194 favourable for the application of hydraulic fracturing.

195 As shown in Fig. 3 and Table 2, mineralogical composition varies among shale
196 intervals. Some of the Permian Dalong shale samples are characterized by higher contents of
197 quartz and calcite and have lower clay mineral contents than average. The pyrite content of
198 most of the samples is generally below the detection level of XRD technology. Nevertheless,

199 some of the Longtan shale samples and others from the Dalong formation exhibit much
200 higher pyrite concentrations that can exceed 10%. Additionally, the clay mineral content of
201 the Ceshui shale samples is generally higher than that from the other two shale intervals.

202 3.2.2 Lithology

203 Based on XRD analysis (Table 2) as well as the structural fabrics identified by thin-
204 section examination (Fig. 4), five primary lithological facies can be distinguished for the
205 shale samples investigated: 1) non-laminated shale, 2) carbonaceous shale, 3) calcareous
206 shale, 4) silty shale, and 5) siliceous shale.

207 Non-laminated shale (Figs. 4b and c) is the most common lithofacies type. Quartz and
208 clay minerals are predominant components, while feldspar and pyrite are relatively rare. The
209 TOC content of non-laminated shale is highly variable, ranging from <1% to >6%.

210 Carbonaceous shale (Figs. 4d and e) is less common than non-laminated shale but is
211 the second most abundant lithofacies type except in the Dalong formation. This lithofacies is
212 dark-coloured and has a high TOC content that is generally >6% (Table 2). The sediments are
213 poorly laminated, and the primary constituents are quartz, clay, pyrite, and organic matter.

214 Calcareous shale is one of the more common lithofacies in shales from the Dalong
215 and Ceshui formations, but it is relatively rare in the Longtan formation (Table 2 and Fig. 4a).
216 The sediments of this lithofacies are typically faintly- to well-laminated depending upon the
217 orientation of the interbedded quartz and organic matter (Fig. 4a). The calcite content in
218 calcareous shale samples accounts for about 30-50%, while TOC content is highly variable,
219 and ranges from <1% to >4% (Table 2).

220 The silty shale is greyish black. It is mainly composed of clay minerals, and a small
221 amount of quartz and feldspar. The TOC content is generally <1%.

222 The siliceous shale is dark-coloured and very hard, and primarily occurs in the Dalong
223 formation. Siliceous shale is characterized by a high quartz content (>85%, Table 2), and the
224 TOC content is commonly higher than that of silty and calcareous shales (Table 2).

225 *3.3 Petrophysical properties*

226 3.3.1 Reservoir storage space

227 SEM analysis was performed on the selected samples to characterize pores and
228 fractures. Organic matter pores, interparticle pores (between grains), intraparticle pores
229 (within mineral grains), and microfractures are all present in the samples (Fig. 5). Organic
230 matter pores (Fig. 5a and b) are well-developed in most of the samples, particularly in high
231 TOC shales. Interparticle pores (Fig. 5b, d and f) can be seen around and between crystals of
232 quartz and feldspar or located within the clay crystals. Intraparticle pores (Figs. 5b–d)
233 primarily occur inside pyrite framboids, and in carbonate- and feldspar-rich samples. Strip-
234 like microfractures often can be seen between clay crystal, or between clay laminae and silty
235 laminae (Figs. 5a, d–e).

236 3.3.2 Porosity and Permeability

237 The results of porosity and permeability analyses are listed in Table 3. Porosity ranges
238 from 0.5% to 14.0% (\bar{x} =6.4%) and permeability ranges from 0.0026 micro Darcy (mD) to
239 0.0640 mD (\bar{x} =0.0130 mD). Shales from the Longtan formation generally have a higher
240 porosity and permeability than samples from the Dalong and Ceshui formations.

241 *3.4 Gas Adsorption Capacity*

242 The high-pressure methane adsorption capacities (i.e., the maximum adsorbed gas
243 amount) for the moisture-equilibrated shale samples vary from 1.24 cm³/g to 4.53 cm³/g
244 (\bar{x} =2.40 cm³/g) (Fig. 6), indicating a strong methane adsorptive potential.

245

246 **4. Discussion**247 *4.1 Organic matter in the shale*

248 TOC represents the richness of organic matter in source rocks. Promising
249 conventional or unconventional source rocks generally have high TOC concentrations (Jarvie
250 et al., 2007). Previous studies have suggested that high pyrite content in shales represents
251 strongly reducing environmental conditions that are favourable for the enrichment and
252 preservation of organic matter (Liang et al., 2014; Tan et al., 2014b, 2015; Wu et al., 2014).
253 As shown in Table 2, shales with high pyrite contents tend to have high TOC contents as well.
254 Given the relatively high TOC contents of the shale samples studied here, this suggests that
255 the analysed transitional shales were most likely deposited in strongly reducing conditions. In
256 fact, transitional sedimentary environments in the study area were dominated by stable and
257 anoxic conditions through the depositional period of the shales (Dang et al., 2016; Liang et al.,
258 2014; Tang et al., 2016). Because the Longtan shale normally exhibits higher TOC and pyrite
259 contents, this formation may have been deposited in more strongly reducing environments
260 compared to shales from the Dalong and Ceshui formations. However, the higher TOC
261 concentration may also indicate a better and/or stronger organic input. According to the
262 results of kerogen typing, the organic matter of the Ceshui shale is dominated by type III
263 kerogen, whereas >70% of the macerals from the Permian shale are type II organics. This
264 suggests that most of the organics found in the Permian shales are derived from marine
265 plankton (i.e., marine microflora and microfauna). However, it has previously been
266 documented that more derived, terrestrial plants were extensively distributed in and near the
267 littoral swamps in this part of China during both the Mississippian and Lopingian (e.g., Ji et
268 al., 2011; Shao et al., 1992). While this suggests that the organic input from terrestrial plants
269 for both the Carboniferous and Permian shales should generally be similar, the observed

270 organic matter in the Permian shale includes much more marine plankton than the
271 Carboniferous shale.

272 *4.2 Favourable geological conditions for natural gas accumulation in shales*

273 4.2.1 Organic geochemistry

274 High TOC content generally suggests that conventional and unconventional
275 petroleum resources are promising for exploration and exploitation (Dang et al., 2016; Jarvie
276 et al., 2007; Tan et al., 2015). TOC values significantly vary among shale reservoirs, but the
277 productive shale gas plays normally exhibit TOC contents >2% (Tan, et al., 2015). Li et al.
278 (2015) reported that the TOC content of the Longtan shale in South China ranges from 0.4%
279 to 14.6%, with a mean of 4.5%. Gu et al. (2015) and Bao et al. (2016) also documented that
280 more than half of analysed Permian shale samples exhibit TOC contents >2%. Compared to
281 productive shale gas plays in the United States, such as the Barnett shale (Dong et al., 2016),
282 and the transitional shales in the Bohai Bay basin and Southern North China basin (Dang et
283 al., 2016; He et al., 2016;), TOC contents of the transitional shales in the study area are even
284 higher. This indicates that the transitional shales in central Hunan have excellent initial
285 potential for petroleum generation.

286 The organic matter type of current exploration targets for shale gas is primarily
287 dominated by type II kerogen (e.g., the Barnett, Marcellus, and Haynesville shale plays in the
288 United States; the shale gas formations in the Western Canadian basin; and the Longmaxi
289 shale in South China) (Dong et al., 2016) (Table 4). Nevertheless, thick, widespread, gas-
290 saturated, fine-grained, organic rich units containing other types of organic matter, which
291 were subjected to extensive biogenic degradation in the thermally immature stage or
292 significant thermal decomposition in the thermally mature or over mature stages, can also
293 serve as excellent exploration targets (Hamblin, 2006; Martini et al., 2003; Tan et al., 2015).
294 The organic matter of the Carboniferous shales in South China have typically been regarded

295 as a type III kerogen (Luo, et al., 2012; Zhang et al. 2014) derived from terrestrial plants. In
296 the Mississippian, organic material in paralic shale and coal seams were both derived from
297 terrestrial plants, including Lycopoids and Equisetoids (Gu et al., 2015; Zhang et al. 2014).
298 However, the coal seams in the Longtan formation are locally distributed across central
299 Hunan, and the shale with high TOC content does not tend to occur within coal seams (Ji et
300 al., 2011). This might be the reason why the organic matter type of the Permian shale differs
301 from that of the Carboniferous shale. Bao et al. (2016) reported that the kerogen $\delta^{13}\text{C}$ values
302 in the Longtan and Dalong shales range from -23‰ to -27‰, further confirming that the
303 organic matter is dominated by type II kerogen, with a minor component of type III kerogen.

304 Most shale gas that is currently produced is primarily a thermogenic gas that was
305 formed by the thermal degradation of organic matter (Tan, et al., 2014c). For example, the
306 highly productive Barnett shale gas play normally has a $R_o > 1\%$, while the Lower Silurian
307 Longmaxi shale in South China has a R_o generally $> 2\%$ (Chen et al., 2011; Tan, et al., 2015;
308 Zhang et al., 2015). Although a minor fraction of shale gas might be of biogenic origin in the
309 thermally immature stage (Martini et al., 2003; Martini et al., 2008), such quantities are
310 significantly less than those of thermogenic shale gas (Tan, et al., 2014c). In addition to the
311 current study, other studies have reported that R_o values of the Longtan and Dalong shales
312 range from 1.1% to 2.4%, with a mean value of 1.6% (Bao et al., 2016; Gu et al., 2015).
313 Zhang et al. (2014) have also documented that the R_o values of the Longtan shale range from
314 1.7% to 2.0%, with a mean value of 1.8%. Compared to the lower Cambrian and Lower
315 Silurian marine shales in or adjacent to the Sichuan basin, which generally exhibit an equal
316 R_o value $> 2.0\%$, the transitional shales studied here are less thermally mature. Interestingly,
317 as shown in Tables 1 and 2, R_o values of the transitional shales increase gradually in strata
318 that are stratigraphically older, indicating a burial depth control on thermal maturity.

319 4.2.2 Mineralogical composition

320 To produce shale gas economically, horizontal drilling and hydraulic fracturing are
321 the most popular choices for completing shale gas wells. The mineralogical composition of
322 shale plays affects both the reservoir quality and well completion quality. Detailed
323 characterization of the mineral constituents is thus critical to the identification of exploration
324 targets, and essential for determining how the shale reservoir should be completed (Tan, et
325 al., 2014b).

326 Mineral compositions are closely related to rock mechanics, and directly determine
327 the brittleness of the rock. The brittleness of shale rocks reflects the capability to fail under
328 pressure, and for cracks to remain open once the rock fractures (Rickman et al., 2008). Brittle
329 shales thus generally respond well to well completion treatments. However, ductile shales,
330 which might be fractured during hydraulic fracturing, can also be easily healed after
331 stimulation. It has been recognized that quartz-rich and clay-low zones are commonly the
332 most brittle intervals within a shale formation (Johnston, 2004). Hydraulic fracturing
333 strategies used in the more brittle zones are reported to enhance the overall gas production of
334 the well (Boyer et al., 2006). More specifically, Bowker (2002) has suggested that the brittle
335 Barnett shale intervals are generally composed of 45% quartz, 27% illite, 8% carbonate, 7%
336 feldspar, 5% pyrite, and 3% siderite.

337 One of the most common methods to determine the brittleness of a shale play is based
338 on relative mineral compositions. Jarvie et al. (2007) and Rickman et al. (2008) documented
339 the correlations between mineral composition and brittleness of the Barnett shales. They
340 reported that the most brittle Barnett shales have high quartz contents, and low clay mineral
341 contents. Conversely, the least brittle shales are rich in clay minerals, with relatively minor
342 amounts of quartz. The shales with abundant carbonate are moderately brittle. However, from
343 a stimulation perspective, not all quartz responses equally during well completion. The most
344 effective quartz component for enhancing brittleness appears to be the recrystallized biogenic

345 opaline silica. Detrital quartz, on the contrary, appears to be less effective (Jarvie et al.,
346 2007). The Brittleness Index was proposed based upon the relative proportions of quartz group
347 minerals (primarily quartz, feldspar, and pyrite), carbonates, and clay minerals, as: Brittleness
348 $\text{Index} = \frac{\text{quartz}}{\text{quartz} + \text{carbonates} + \text{clays}}$ (Jarvie et al., 2007). Selecting zones in a shale
349 interval that are relatively more brittle is of importance for developing fractures that are large
350 enough to connect the largest rock volume to the wellbore during the well completion
351 process. The geometry of fractures created in brittle shales is different from that of ductile
352 shales. The stimulation treatments carried out on brittle shales can create large, complex
353 fracture networks that expose a large amount of shale surface area, and thus enable
354 commercial gas production (Grieser and Bray, 2007).

355 Mineral compositions are also important for fluid selection during well completion.
356 The determination of mineralogy and fluid sensitivity is essential for optimizing completion
357 and stimulation strategies (Britt and Schoeffler, 2009). In most cases, acid is commonly used
358 to dissolve soluble minerals, increase porosity, and improve the fracturing process. Because
359 carbonate minerals can be easily dissolved even in weak acid solutions, the contents of
360 carbonates evidently correlate with the acid solubility of shale samples (Rickman, et al.,
361 2008). If samples have low carbonate concentrations, they generally show low to moderate
362 acid solubility. In that scenario, mixed fluids of weak acids and surfactants are recommended
363 to roughen the fracture surfaces, increase surface areas, and prevent significant generation of
364 fines that could cause plugging of the fractures created, and damage to perforations
365 (Rickman, et al., 2008). On the other hand, clay swelling is a significant problem for the
366 stability of boreholes and created fractures, and finally on the gas recovery from shale
367 reservoirs. If more smectite or illite/smectite mixed layers are present, the swelling potential
368 of the shale might be substantial. In this case, development then requires more protective
369 strategies, and more rigorous evaluation before the initiation of hydraulic fracturing.

370 The average quartz and clay mineral contents of Permian shales in South China are
371 commonly >50%, and <25%, respectively (Zhang et al., 2016). Meanwhile, Carboniferous
372 shales in the same region exhibit quartz and clay mineral contents of ~60.8% and ~23.3%,
373 respectively (Miao et al. 2016). The highly productive lower Palaeozoic marine shales in
374 South China and the transitional shales in Palaeozoic basins in North China generally contain
375 highly brittle mineral contents (> 60% on average), and low clay mineral contents (< 40% on
376 average) (Chen et al., 2011; Ding et al., 2013; Tan et al., 2014b; Tang et al., 2014; Zhang et
377 al., 2015). Our study also indicates mineral compositions in transitional Carboniferous and
378 Permian shales in South China that are dominated by brittle minerals. These findings could
379 provide valuable insights for reservoir evaluation and stimulation treatments in the future.

380 4.2.3 Petrophysics

381 Intercrystallite pores in pyrite framboids commonly exist in shale samples, and
382 contribute to gas storage (Loucks et al., 2009, 2012). For the analysed transitional shale
383 intervals, pyrite was relatively abundant in shales from the Longtan formation, thus
384 intraparticle pores occur more frequently (Fig. 5b). Intraparticle pores occur in shale samples
385 with relatively high carbonate and/or feldspar contents (Figs. 5b–d). This can be ascribed to
386 the partial dissolution of soluble carbonate and feldspar minerals (Heath, et al., 2011; Loucks
387 et al., 2012). Microfractures (Figs. 5e), which can be formed during catagenesis, are well
388 developed in shale samples with high clay mineral contents (i.e., illitisation could result in
389 microfractures in shale with lengths up to tens of micrometres) (Liang et al., 2014).

390 Previous studies have shown that the average porosity and permeability of the
391 Permian shales in the study area are <2% and ~0.007 mD, respectively (Gu et al., 2015; Bao
392 et al., 2016), whereas the porosity of the Carboniferous Ceshui shale ranges from 1% to 6.2
393 %, with a mean value of 3.5% (Miao, et al., 2016). Compared with these results, porosity and
394 permeability values obtained for the shale samples in our investigation are generally higher

395 (Table 3). One of the primary reasons might be that some of the shale samples in the current
396 study have higher TOC contents, and well-developed micro-fractures. As our samples were
397 freshly collected, weathering impact on petrophysical properties should be low. However, our
398 findings suggest that these shale intervals are all characterized by low porosity and ultra-low
399 permeability, which may result in an even tighter reservoir than the Barnett shale (Dong, et
400 al., 2016).

401 To analyse the primary drivers of porosity formation, we examined the correlation
402 between porosity and TOC content (Fig. 7a). There is a positive correlation between TOC
403 content and porosity for most of the selected samples. This suggests that organic matter
404 probably dominates the porosity of the shale. This might also be the reason why the porosity
405 of the Longtan shale is comparatively higher than the less organic-rich shales from the
406 Dalong and Ceshui formations (Table 3). Additionally, there is a negative relationship
407 between the porosity and density (Fig. 7b). This phenomenon might be related to organic
408 matter content because the density of shale tends to decrease as TOC contents increase (Fig.
409 7c). However, a few of the selected samples have higher porosity and permeability, even
410 though they have relatively low TOC (e.g., sample LSJ05; Tables 2 and 3). Through SEM
411 analysis, we found that these samples generally have well developed microfractures (e.g.
412 LSJ05; see Fig. 5e). This could suggest that microfractures can be an important contributor to
413 porosity. For the Barnett shale, microfractures provide migration pathways, and reservoir
414 space for the accumulation of shale gas (Liang et al., 2014; Loucks et al., 2012). However, in
415 this study, correlations between porosity and mineral constituents (e.g. quartz and clay
416 minerals) of the shale remain unclear, and this is likely due to the heterogeneity of the shales.

417 In general, shales exhibit significant anisotropic properties from the nanometre scale
418 to the reservoir scale (e.g., organic and inorganic constituents, mineral types, and structures).
419 For low TOC samples, mineral-associated pores should be dominant. Nevertheless, the

420 contribution of organic matter host pores becomes significant if TOC content rises and
421 thermal maturity increases to the gas window. According to research performed on the highly
422 mature (dry gas window) Longmaxi shale in South China, most of the pores in that unit are
423 mineral pores when TOC is less than 0.9%. The contribution of mineral pores is similar to
424 that of organic pores when TOC is in the range of 0.9-1.7%, and organic pores are more
425 significant than mineral pores when TOC is higher than 1.7% (Tang et al., 2016). However,
426 the Barnett shale samples that span a maturity range from a later wet gas window to a dry gas
427 window indicate a positive correlation between TOC and porosity for samples with TOC
428 <5.5%, and little or no correlations for samples with TOC >5.5% (Milliken, et al., 2013).
429 Since quartz, carbonates, and clay minerals are the principal mineral constituents of shales,
430 their relative concentrations can significantly influence porosity because clay minerals are
431 porous, while carbonates can be easily dissolved by geofluids (Ross and Bustin, 2009). In
432 some shales, the pyrite content can be greater than 10%, and pyrite framboids are commonly
433 present. In that context, pyrite-associated pores may also be important.

434 Shales are slowly deposited through suspension in calm waters, and this long
435 deposition period can result in strong vertical heterogeneity in both composition and
436 structure. Lamina, thin sand layers, and bioclasts all vary over time in the investigated shale
437 intervals. As revealed by Pan et al. (2015b), in addition to organic and inorganic constituents,
438 the heterogeneous layering structures in different directions in shales strongly impact porosity
439 and permeability, resulting in anisotropic petrophysical properties. However, porosity and
440 permeability measurements are generally performed on small sample pieces or plugs, and the
441 obtained results are very sensitive to experimental conditions. Therefore, accounting for the
442 petrophysical properties of shales at a large scale requires a very large sample size from
443 across the vertical and spatial extents of the unit. Additional studies with larger sample sizes
444 are needed in the future.

445 4.2.4 Methane adsorption capacity

446 Research by Bao et al. (2016) has previously shown that the average methane
447 adsorption capacity of the Permian Longtan and Dalong shales are 2.7 and 3.5 cm³/g,
448 respectively, exhibiting a relatively strong gas adsorptive potential. Nevertheless, the
449 Carboniferous-Permian shale intervals have lower methane adsorption capacity compared to
450 the lower Cambrian and lower Silurian marine shales in or adjacent to the Sichuan basin,
451 South China (Tan et al., 2014a; Zhang et al., 2015). The gas adsorption capacity of over
452 mature marine shales is positively correlated with TOC content (Chalmers et al., 2008;
453 Gasparik et al., 2014; Han et al., 2013; Tan et al., 2014a; Wu et al., 2014). However, as
454 shown in Fig. 7, the methane adsorption capacity of TOC-rich samples (i.e. DLS02 and
455 DBQ09) is not always significantly higher than that of TOC-poor samples (i.e. NT02) for the
456 high maturity shales of this study. This suggests that other factors may play more important
457 roles in influencing methane adsorption.

458 Shale samples with Ro values less than 1.5% (i.e., samples DLS02 and DBQ09; Fig. 6)
459 have low gas adsorption capacity irrespective of their TOC values. However, when Ro values
460 of the shale samples are greater than 1.5% (i.e., samples NT02 and JZS09; Fig. 6), their gas
461 adsorption capacity is much higher than that of the shale samples with Ro values <1.5%. This
462 suggests that the gas adsorption capacity might be closely associated with thermal maturity
463 for the high maturity shales. Compared with the two samples with Ro values above 1.5% (i.e.,
464 samples DLS02 and DBQ09; Fig. 6), even when there is little difference in thermal maturity,
465 the gas adsorption capacity of the shale increases greatly with higher TOC content. This
466 implies that the organic matter content might be largely responsible for adsorbing gas in the
467 high maturity range.

468 Micropores hosted in organic matter are the primary factor that influences the
469 adsorption capacity of organic-rich rocks (Loucks, et al., 2012; Tan, et al., 2014a; Tan, et al.,

2014b; Zhang et al., 2015; Zhong et al., 2016). However, micropores are poorly developed during the low maturity to oil window range ($R_o=0.5-1.0\%$) but increase dramatically as thermal maturity enters the gas window stage ($R_o \geq 1.5\%$) (Xiong et al., 2015). Additionally, organic matter type possibly influences the adsorption capacity of shale and coal samples (Gasparik et al., 2014; Tan et al., 2014a;). The transitional shales in the current study contain moderate amounts of type III organic matter, while the lower Cambrian and lower Silurian marine shales in South China lack type III kerogen. The relatively lower adsorption capacity of the analysed transitional shales can be partially ascribed to the different types of organic matter.

The Xiangye-1 well in the study area is the first and, presently, the only natural gas exploration well targeted toward the studied transitional shales (Bao et al., 2016; Gu et al., 2015). During drilling, the Dalong formation shale exhibited very low desorption gas content that was attributed to poor preservation conditions, long periods of tectonic alteration, and extensive thermal evolution (Bao et al., 2016; Gu et al., 2015). Based on the above discussion, the low gas content might also result from the low thermal maturity given that shales with $R_o < 1.5\%$ generally have less gas adsorption capacity. As shown in Tables 1 and 2, the R_o values for most of the Dalong formation shale samples are $< 1.5\%$. The intrinsic reason is that micropores might be relatively less developed in a low thermal maturity range. It should be noted that extrapolations from adsorption data obtained in the lab to *in situ* subsurface geological conditions requires a more comprehensive, multi-factor analysis.

In addition to the inherent properties of shales (e.g., organic matter content, mineral constituents, thermal maturity, and pore structure), *in situ* geological conditions of shale reservoirs are fraught with uncertainties. For example, gas adsorption measurements are generally performed in isothermal conditions, whereas the geological temperature varies in reservoirs at different depths. The simulated applied pressure is likely much lower than actual

495 reservoir pressures, given that the burial depth of some of the shale gas reservoirs in South
496 China exceeds 5 km. The moisture content also varies markedly with diagenesis and thermal
497 maturation of organic matter. Moreover, gas adsorption measurements are commonly
498 performed on cuttings or powders that show higher pore surface accessibility than the intact
499 shales underground.

500 Nevertheless, experimental adsorption data provide the basis for GIP estimation,
501 particularly for regions where natural gas production has not yet been achieved, and
502 desorption data are very rare (Gasparik, et al., 2014). The uncertainty of GIP estimation
503 resulting from both inherent and exogenic factors can be controlled through adsorption
504 experiments performed on a number of representative samples, and under a variety of lab
505 conditions, and with enhanced knowledge of the *in situ*, underground geological conditions of
506 shale reservoirs (Gasparik, et al., 2014).

507

508 **5. Conclusions**

509 We conducted a variety of analyses on Carboniferous and Permian transitional shale
510 samples from central Hunan to investigate their natural gas potential. Our primary findings
511 are:

- 512 1. These shale intervals are abundant in organic matter and were deposited in reducing
513 sedimentary environments. The organic matter type of the Ceshui shale is dominated
514 by type III kerogen, while that of the Permian shale is principally type II. The thermal
515 maturities of the shales have entered into the late wet gas and dry gas window stages,
516 respectively.
- 517 2. Non-laminated and carbonaceous shale are the dominant lithological types, followed
518 then by calcareous shale, silty shale, and siliceous shale. Quartz and clay minerals are

519 the principal constituents. Pyrite is highly concentrated in certain Permian shale
520 samples, and generally coincides with higher TOC contents.

521 3. Four types of pore structures were identified through SEM analysis (i.e., organic
522 matter pores, interparticle pores, intraparticle pores, and microfractures). The mean
523 porosity for all sample is 6.4%, and the mean permeability is 0.013 mD. TOC and
524 well-developed microfractures can greatly affect the porosity and permeability of the
525 shale.

526 4. The gas adsorption capacity of the transitional shales was found to vary from 1.24
527 cm^3/g to 4.53 cm^3/g , with a mean value of 2.40 cm^3/g under the experimental
528 conditions. Meanwhile, shales with high TOC content and $R_o > 1.5\%$ exhibit high gas
529 adsorption capacity.

530

531 **Acknowledgements**

532 This work is supported by the Open Fund (PLC201302) of the State Key Laboratory of
533 Oil and Gas Reservoir Geology and Exploitation (Chengdu University of Technology), Major
534 Project of Hunan Provincial Science and Technology Bureau (2012FJ1006), the Open Fund
535 (E21645) of the Hunan Key Laboratory of Shale Gas Resource Utilization (Hunan University
536 of Science and Technology), and the Innovation Program of Central South University
537 (502501005). We thank Jeffrey Dick for editing the language. Zhenghui Xiao also
538 acknowledges support from the China Scholarship Council (CSC).

539

540 **Appendix**

541 1. Type III kerogen is derived from terrestrial plant debris, much of which remains
542 taxonomically identifiable. Additionally, type III kerogens mostly contain condensed

543 polyaromatics and oxygenated functional groups, with minor aliphatic chains (Tissot and
544 Welte, 1984).

545 2. Type II kerogen is typically derived from a mixture of phytoplankton, zooplankton,
546 and microorganisms (bacteria) that have been deposited in a reducing environment. Though
547 type II kerogens may also include terrestrial debris (pollen spores, plant cuticle, etc.), they are
548 most often found in marine sediments characterized by autochthonous organic matter (Tissot
549 and Welte, 1984).

550

551 **References**

552 Bao, S.J., Lin, T., Nie, H.K., Ren, S.M., 2016. Preliminary study of the transitional facies
553 shale gas reservoir characteristics: Taking Permian in the Xiangzhong Depression as an
554 example. *Earth Science Frontiers* 23, 44–53.

555 Bowker, K.A., 2007. Barnett Shale gas production, Fort Worth Basin: issues and discussion.
556 *AAPG Bulletin* 91, 523–533.

557 Boyer C, Kieschnick J, Lewis R., 2006. Producing gas from its source. *Oilfield Review*, 18,
558 36-49.

559 Britt, L., Schoeffler, J., 2009. The geomechanics of a shale play: What makes a shale
560 prospective. In SPE Eastern Regional Meeting. *Society of Petroleum Engineers* 125525, 1-
561 9.

562 Bu, H., Ju, Y., Tan, J., Wang, G., & Li, X., 2015. Fractal characteristics of pores in non-
563 marine shales from the Huainan coalfield, eastern China. *Journal of Natural Gas Science*
564 *and Engineering* 241, 66-177.

565 Chalmers, G.R.L., Bustin, R. M., 2008. Lower Cretaceous gas shales in northeastern British
566 Columbia. Part I: Geological controls on methane sorption capacity. *Bulletin of Canadian*
567 *petroleum geology* 56, 1–21.

- 568 Chen, S.B., Zhu, Y.M., Wang, H.Y., Liu, H.L., Wei, W., Fang, J.H., 2011. Shale gas
569 reservoir characterization: a typical case in the southern Sichuan Basin of China. *Energy*
570 36, 6609–6616.
- 571 Dang, W., Zhang, J.C., Tang, X., Chen, Q., Han, S.B., Li, Z.M., Du, X.R., Wei, X.L., Zhang,
572 M.Q., Liu, J., Peng, J.L., Huang, Z.L., 2016. Shale gas potential of Lower Permian
573 marine–continental transitional black shales in the Southern North China Basin, central
574 China: Characterization of organic geochemistry. *Journal of Natural Gas Science and*
575 *Engineering* 28, 639–650.
- 576 Ding, W.L., Zhu, D.W., Cai, J.J., Gong, M.L., Chen, F. Y., 2013. Analysis of the
577 developmental characteristics and major regulating factors of fractures in marine–
578 continental transitional shale–gas reservoirs: A case study of the Carboniferous–Permian
579 strata in the southeastern Ordos Basin, central China. *Marine and Petroleum Geology* 45,
580 121–133.
- 581 Dong, D.Z., Wang, Y.M., Huang, X.N., Zhang, C.C., Guan, Q.Z., Huang, J.L., Wang, S.F., Li,
582 X.J., 2016. Discussion about geological characteristics, resource evaluation methods and
583 its key parameters of shale gas in China. *Natural Gas Geoscience* 27, 1583–1601.
- 584 Feng, Z.Z., He, Y.B., Wu, S.H., 1993. Lithofacies paleogeography of Permian Middle and
585 Lower Yangtze region. *Acta Sedimentologica Sinica* 11, 13–24.
- 586 Gasparik, M., Bertier, P., Gensterblum, Y., Ghanizadeh, A., Krooss, B. M., Littke, R., 2014.
587 Geological controls on the methane storage capacity in organic–rich shales. *International*
588 *Journal of Coal Geology* 123, 34–51.
- 589 Grieser, W., Bray, J. 2007. Identification of Production Potential in Unconventional
590 Reservoirs. Society of Petroleum Engineers. doi:10.2118/106623-MS

- 591 Gu, Z.X., Peng, Y.M., He, Y.B., Hu, Z.Q.; Zhai, Y.J., 2015. Geological conditions of
592 Permian sea–land transitional facies shale gas in the Xiangzhong depression. *Geology in*
593 *China* 42, 288–299.
- 594 Hamblin, A.P., 2006. The “Shale Gas” concept in Canada: A preliminary inventory of
595 possibilities. *Geological Survey of Canada* 5384:108.
- 596 Han, S.B., Zhang, J.C., Li, Y.X., Horsfield, B., Tang, X., Jiang, W.L., Chen, Q., 2013.
597 Evaluation of lower Cambrian shale in Northern Guizhou Province, South China:
598 implications for shale gas potential. *Energy & Fuels* 27, 2933–2941.
- 599 He, J.H., Ding, W.L., Zhang, J.C., Li, A., Zhao, W., Dai, P., 2016. Logging identification and
600 characteristic analysis of marine–continental transitional organic–rich shale in the
601 Carboniferous–Permian strata, Bohai Bay Basin. *Marine and Petroleum Geology* 70, 273–
602 293.
- 603 Heath J.E., Dewers T.A., McPherson B.J., Petrusak R., Chidsey, Jr. T.C., Rinehart A.J.,
604 Mozley, P.S., 2011. Pore networks in continental and marine mudstones: Characteristics
605 and controls on sealing behavior. *Geosphere* 7, 429–454.
- 606 Jarvie, D.M., Hill, R.J., Ruble, T.E., Pollastro, R.M., 2007. Unconventional shale–gas
607 systems: the Mississippian Barnett Shale of north–central Texas as one model for
608 thermogenic shale–gas assessment. *AAPG Bulletin* 91, 475–499.
- 609 Ji, C.W., Shao, L.Y., Peng, Z.Q., 2011. Late permian sequence–paleogeography and coal
610 accumulation in Hunan province. *Journal of China University of Mining & Technology* 40,
611 103–110.
- 612 Ji, W. M., Song, Y., Jiang, Z. X., Wang, X.Z., Bai, Y.Q., Xing, J. Y., 2014. Geological
613 controls and estimation algorithms of lacustrine shale gas adsorption capacity: a case study
614 of the Triassic strata in the southeastern Ordos Basin, China. *International Journal of Coal*
615 *Geology* 134, 61–73.

- 616 Jing, L., Pan, J.P., Xu, G.S., Ma, R.L., Yuan, H.F., Luo, X.P., Wu, C.R., 2013. Lithofacies
617 paleogeography characteristics of the marine shale series of strata in the Xiangzhong–
618 Xiangdongnan depression, Hunan, China. *Journal of Chengdu University of Technology*
619 39, 215–222.
- 620 Johnston, D., 2004. Technological advances expand potential pay. *Oil and Gas Journal*, 102,
621 51-59.
- 622 Li, G.L., Wang, X.H., Bo, D.Y., Luo, P., Jiang, W., 2015. Potentiality exploration of the
623 Upper Permian Longtan formation shale gas in central and southeastern Hunan Province.
624 *Geological Science and Technology Information* 34, 133–138.
- 625 Li, H.T., Cao, D.Y., Wang, L.J., Guo, A.J., Li, Y.F., Xu, Hao. 2013. Characteristics and
626 evolution of coal-controlled structures on the east slope of the Xuefengshan Domain in
627 central Hunan province. *Geotectonica et Metallogenia* 37,611-621.
- 628 Liang, C., Jiang, Z.X., Zhang, C.M., Guo, L., Yang, Y.T., Li, J., 2014. The shale
629 characteristics and shale gas exploration prospects of the Lower Silurian Longmaxi shale,
630 Sichuan Basin, South China. *Journal of Natural Gas Science & Engineering* 21, 636–
631 648.
- 632 Liang, J.J., Ma, R.L., Bu, S.F., Liu, W.J., Yang, C., 2014. Reservoir characteristics of shale in
633 Xiangzhong depression and Xiangdongnan depression of Hunan, China. *Journal of*
634 *Chengdu University of Technology* 41, 45–54.
- 635 Loucks, R. G., Reed, R. M., Ruppel, S. C., Jarvie, D. M., 2009. Morphology, genesis, and
636 distribution of nanometer-scale pores in siliceous mudstones of the Mississippian Barnett
637 Shale. *Journal of Sedimentary Research* 79, 848–861.
- 638 Loucks, R.G., Reed, R.M., Ruppel, S.C., Hammes, U., 2012. Spectrum of pore types and
639 networks in mudrocks and a descriptive classification for matrix-related mudrock pores.
640 *AAPG Bulletin* 96, 1071–1098.

- 641 Luo, X.P., Liu, J., Xu, G.S., Ma, R.L., Xian, Z.Y., Xu, M., 2012. Geochemical characteristics
642 and isothermal adsorption properties of the Devonian–Carboniferous marine mud shale in
643 the Xiangzhong depression, Hunan, China. *Journal of Chengdu University of*
644 *Technology* 39, 206–214.
- 645 Martini, A. M., Walter, L. M., McIntosh, J. C., 2008. Identification of microbial and
646 thermogenic gas components from Upper Devonian black shale cores, Illinois and
647 Michigan basins. *AAPG Bulletin* 92, 327-339.
- 648 Martini, A.M., Walter, L.M., Ku, T.C.W., Budai, J.M., McIntosh, J.C., Schoell, M., 2003.
649 Microbial production and modification of gases in sedimentary basins: A geochemical
650 case study from a Devonian shale gas play, Michigan basin. *AAPG Bulletin* 87, 1355–
651 1375.
- 652 Pan, Z. and Connell, L.D. 2015. Reservoir simulation of free and adsorbed gas production
653 from shale. *Journal of Natural Gas Science and Engineering* 22, 359-370.
- 654 Pan, Z., Ma, Y., Connell, L. D., Down, D. I., and Camilleri, M. 2015. Measuring anisotropic
655 permeability using a cubic shale sample in a triaxial cell. *Journal of Natural Gas Science*
656 *and Engineering*, 26, 336-344.
- 657 Rickman, R., Mullen, M. J., Petre, J. E., Grieser, W. V., & Kundert, D. 2008. A practical use
658 of shale petrophysics for stimulation design optimization: All shale plays are not clones of
659 the Barnett Shale. Society of Petroleum Engineers. doi:10.2118/115258-MS
- 660 Shao, L.Y., Zhang, P.F., Liu, Q.F., Zheng, M.J., 1992. The Lower Carboniferous Ceshui
661 Formation in central Hunan, South China: depositional sequences and episodic coal
662 accumulation. *Geological Review* 38, 52–58.
- 663 Slatt, R.M., O'Brien, N.R. 2011. Pore types in the Barnett and Woodford gas. *AAPG Bulletin*
664 95, 2017–2030.

- 665 Tan, J. Q., Weniger, P., Krooss, B., Merkel, A., Horsfield, B., Zhang, J. C., Boreham, C. J.,
666 Graas, G. V., Tocher, B. A., 2014a. Shale gas potential of the major marine shale
667 formations in the Upper Yangtze Platform, South China, Part II: Methane sorption
668 capacity, *Fuel* 129, 204–218.
- 669 Tan, J.Q., Horsfield, B., Fink, R., Krooss, B., Schulz, H. M., Rybacki, E., Zhang, J.C.,
670 Boreham, C. J., Graas, G.V., Tocher, B.A., 2014b. Shale gas potential of the major marine
671 shale formations in the Upper Yangtze platform, South China, Part III: mineralogical,
672 lithofacial, petrophysical, and rock mechanical properties. *Energy Fuels* 28, 2322–2342.
- 673 Tan, J.Q., Horsfield, B., Mahlstedt, N., Zhang, J.C., diPrimio, R., Vu, T. A. T., Boreham,
674 C. J., Graas, G. V., Tocher, B. A., 2013. Physical properties of petroleum formed during
675 maturation of Lower Cambrian shale in the upper Yangtze Platform, South China, as
676 inferred from PhaseKinetics modelling. *Marine & Petroleum Geology* 48, 47–56.
- 677 Tan, J.Q., Horsfield, B., Mahlstedt, N., Zhang, J.C., Boreham, C. J., Hippler, D., Graas, G. V.,
678 Tocher, B. A., 2015. Natural gas potential of Neoproterozoic and lower Palaeozoic marine
679 shales in the Upper Yangtze Platform, South China: geological and organic geochemical
680 characterization. *International Geology Review* 57, 305-326.
- 681 Tang, S., Zhang, J.C., Elsworth, D., Tang, X., Li, Z. M., Du, X. R., Yang, X.Q., 2016.
682 Lithofacies and pore characterization of the Lower Permian Shanxi and Taiyuan shales in
683 the southern North China Basin. *Journal of Natural Gas Science & Engineering* 36, 644–
684 661.
- 685 Tang, X., Zhang, J.C., Wang, X.Z., Yu, B.S., Ding, W.L., Xiong, J.Y., Yang, Y.T., Wang,
686 L., Yang, C., 2014. Shale characteristics in the southeastern Ordos Basin, China:
687 implications for hydrocarbon accumulation conditions and the potential of continental
688 shales. *International Journal of Coal Geology* 128, 32–46.
- 689 Tissot B P, Welte D H. 1984. Petroleum Formation and Occurrence. Springer-Verlag, 1984.

- 690 Wang, J., Li, S.Z., Jin, C., Wang, Y.J., Zhang, G.W., Liu, L.P., Liu, X. 2010. Dome-and-
691 basin pattern in central Hunan province: stages and genesis of fold superposition.
692 *Geotectonica et Metallogenia* 34, 159-165.
- 693 Wang, M.Y., Guo, J.L., Kuang, L.X., Zhu, T., 2010. Geochemical characteristics and
694 evolution of the hydrocarbon source rocks from Lianyuan Depression in the middle of
695 Hunan province. *Natural Gas Geoscience* 21, 721–726.
- 696 Wu, Y., Fan, T.L., Zhang, J.C., Jiang, S., Li, Y.F., Zhang, J.P., Xie, C., 2014.
697 Characterization of the upper Ordovician and lower Silurian marine shale in northwestern
698 Guizhou province of the upper Yangtze block, South China: Implication for shale gas
699 potential. *Energy Fuels* 28, 3679–3687.
- 700 Xiong, J.Y., Li, S.T., Tang, X., Chen, R.Y., Wang, M., Huang, Z.L., Sun, X.N., Du, K.F.,
701 2015. Organic matter occurrence and microscopic mechanism of pore formation in the
702 lacustrine tight carbonate reservoirs. *Oil & Gas Geology* 36, 756–765.
- 703 Xu, F.H., Qian, J., Yuan, H.F., Xu, G.S., Liang, J.J., 2015. Sedimentary mode and reservoir
704 properties of mud shale series of strata in Xiangzhong–Xiangdongnan depression, Hunan,
705 China. *Journal of Chengdu University of Technology* 42, 80–89.
- 706 Xu, Y.G., Qi, K.L., 2005. Reconsideration on marine petroleum exploration prospects in the
707 middle Hunan depression. *Petroleum Geology & Experiment* 27, 594–596.
- 708 Zhan, G.J., Liu, G.X., Guan, H.L., Fang, C.M., Deng, M., 2006. Genetic types of natural gas
709 of Xiangzhong depression. *Natural Gas Geoscience* 21, 721–726.
- 710 Zhang, C.L., Tang, S.H., Fan, E.P., Wang, S.B., Sun, C.H., Sun, J.J., 2014. Shale gas
711 reservoir characteristics of Longtan Formation in Lianyuan Depression. *Journal of Oil &*
712 *Gas Technology* 36, 32–36.

- 713 Zhang, G, T, Chen, X, H., Zhang, B. M., Li, H., 2016. Physical property characteristics of
714 Permian shale reservoir in the Shaoyang Depression, central Hunan province.
715 *Geology and Mineral Resources of South China* 32, 149–158.
- 716 Zhang, J.P., Fan, T.L., Li, J., Zhang, J.C., Li, Y.F, Wu, Y., Xiong, W.W., 2015.
717 Characterization of the Lower Cambrian Shale in the Northwestern Guizhou Province,
718 South China: Implications for Shale–Gas Potential. *Energy Fuel* 29, 6383–6393.
- 719 Zhang, L.T., Guo, J.H., Jiao, P., Zhang, Z., 2014. Accumulation conditions and exploration
720 potential of shale gas of Lower Carboniferous in Lianyuan Depression in the middle of
721 Hunan Province. *Journal of Central South University* 45, 2268–2277.
- 722 Zhong, J.A., Chen, G.J., Lv, C.F., Yang, W., Xu, Y., Yang, S., Xue, L.H., 2016.
723 Experimental study of the impact on methane adsorption capacity of continental shales
724 with thermal evolution. *Journal of Natural Gas Geoscience* 1, 165–172.
- 725 Zhou, X.K., Guo, J.H., 2014. Petroleum accumulation characteristics and preservation
726 conditions of Lianyuan sag in the central Hunan. *Journal of Geomechanics* 20, 222–229.
- 727 Zhu, W., Yi, J.Z., 2012. Analyses on the complex geologic structure and its gas exploration
728 potential in Lianyuan region of middle Hunan province. *Special Oil & Gas Reservoirs* 19,
729 35–38.
- 730 Zou, C.N., Dong, D.Z., Wang, S.J., Li, J.Z., Li, X.J., Wang, Y.M., Li, D.H., Chen, K.M.,
731 2010. Geological characteristics, formation mechanism and resource potential of shale gas
732 in China. *Petroleum Exploration and Development* 6, 641–653.

733

734 **Fig. 1.** (a) Outline map of China showing position of Hunan Province and study area. (b)
735 Regional geological map of the study area and sampling locations. (c) Generalized
736 stratigraphic column of Carboniferous-Permian strata of the study area with stars marking
737 position of target shales (modified from Jing et al., 2013).

738

739 **Fig. 2.** Structural geology map of central Hunan (Modified from Li et al. 2013)

740

741 **Fig. 3.** Ternary diagram of mineralogical constituents.

742

743 **Fig. 4.** Petrological images of Carboniferous-Permian transitional shale samples from the
744 study area. (a) Calcareous shale (QXJ05) from the Lopingian aged Dalong formation at the
745 Qixingjie section. Quartz and carbonate concentrate in white laminae, while clay and organic
746 matter concentrate in black laminae. (b) Non-laminated shale (DPQ06) from the Lopingian
747 aged Dalong formation at the Duanpoqiao section; dark area is mainly composed of organic
748 matter and clay, while the light area primarily comprises quartz and feldspar. (c) Non-
749 laminated shale (NT02) from the Lopingian aged Longtan at the Nantang section; dark area
750 consists of organic matter and clay, and the light is mainly quartz. (d) Carbonaceous shale
751 (DLS05) from the Lopingian aged Longtan formation at the Doulishan section; dark area is
752 mainly organic matter and clay, and the light is mainly quartz and feldspar. (e) Silty shale
753 (LMJ06) from the Mississippian aged Ceshui formation at the Lumaojiang section; clay
754 minerals occupy a large area in the texture, while organic matter and quartz are scattered
755 amongst the matrix. (f) Carbonaceous shale (LSJ04) from the Mississippian aged Ceshui
756 formation at the Liangshuijing section; dark area is mainly organic matter and light area is
757 mainly quartz. Organic matter aggregates or particles are randomly distributed in the matrix.

758

759 **Fig. 5.** SEM images of Carboniferous-Permian transitional shale samples from the study
760 area. (a) Carbonaceous shale (LSJ04) from the Mississippian aged Ceshui formation at the
761 Liangshuijing section; “honeycomb” organic pores and micro-fractures are well developed.
762 (b) Carbonaceous shale (DLS05) from the Lopingian aged Longtan formation at the

763 Doulishan section; interparticle pores exist between pyrite framboids or between pyrite
764 crystals and clay flakes. Intra-particle pores in the feldspar minerals and “honeycomb”
765 organic-matter pores generated by hydrocarbon expulsion are well developed. (c) Calcareous
766 shale (QXJ02) from the Lopingian aged Dalong formation at the Qixingjie section;
767 intraparticle pores in the carbonate minerals are well developed. (d) Transitional shale
768 (DPQ03) from the Lopingian aged Dalong formation at the Duanpoqiao section; inter-
769 particle pores occur between quartz minerals, intra-particle pores exist in the feldspar
770 minerals and micro-fractures in clay minerals and at weak interfaces are well developed. (e)
771 Carbonaceous shale (LSJ05) from the Mississippian aged Ceshui formation at the
772 Liangshuijing section; micro-fractures between clay flakes or between clay laminae and silty
773 laminae are well developed. (f) Silty shale (LMJ06) from the Mississippian aged Ceshui
774 formation at the Lumaojiang section; micro-fractures between clay flakes are well developed.

775

776 **Fig. 6.** Methane adsorption isotherms at 40 °C

777

778 **Fig. 7.** Correlation plots for Carboniferous-Permian shale samples in Central Hunan Province
779 plotting (a) porosity with TOC content, (b) porosity with density, and (c) TOC content with
780 density.

781

782 **Table 1.** TOC and Ro values from the Carboniferous-Permian transitional shale in central
783 Hunan.

784

785 **Table 2.** Results of TOC, Ro and XRD mineralogy for some representative transitional shale
786 samples from central Hunan.

787

788 **Table 3.** Rock density, porosity, and permeability for Carboniferous–Permian transitional
789 shale in central Hunan.

790

791 **Table 4.** Comparison of the shale gas reservoir rocks in central Hunan with other worldwide
792 shale gas source rocks. Setting = depositional environment of source rocks; TOC – Total
793 Organic Carbon; Kerogen = Kerogen Type; Ro = Vitrinite reflectance values; GAC = Gas
794 adsorbtion capacity. Data for Ceshui, Dalong and Longtan shales from this paper; sources for
795 other data from the study by Dong et al. (2016).

Tables

Table 1. TOC and Ro of Carboniferous–Permian shale in central Hunan

Formation	Sections(code)	TOC (%)			Ro (%)		
		Min value	Max value	Mean value	Min value	Max value	Mean value
Dalong	Shimingqiao(SMQ)	0.4	5.0	3.3	1.1	1.4	1.3
Dalong	Qixingjie(QXJ)	0.6	4.6	2.3	1.2	1.7	1.4
Dalong	Duanpoqiao(DPQ)	0.9	6.6	4.8	1.2	1.8	1.5
Dalong	Tantou(TT)	0.5	4.8	2.2	1.2	1.7	1.5
	avg.	0.6	5.3	3.2	1.2	1.7	1.4
Longtan	Qixingjie(QXJ)	0.8	8.8	4.4	1.2	1.9	1.5
Longtan	Doulishan(DLS)	6.9	8.8	7.8	1.4	1.5	1.4
Longtan	Nantang(NT)	2.4	5.3	4.0	1.1	1.6	1.4
Longtan	Jilong(JL)	2.6	9.2	6.0	1.6	1.9	1.7
Longtan	Tantou(TT)	1.8	6.2	3.6	1.1	1.9	1.6
	avg.	2.9	7.7	5.2	1.3	1.8	1.5
Ceshui	Jingzhushan(JZS)	0.8	6.1	2.4	1.3	2.8	1.8
Ceshui	Zhaoyang(ZY)	2.2	9.0	4.5	1.6	2.2	1.9
Ceshui	Liangshuijing(LSJ)	0.4	7.4	1.8	1.5	2.4	2.1
Ceshui	Xiandong(XD)	0.4	1.6	1.2	1.4	1.8	1.7
Ceshui	Lumaojiang(LMJ)	0.7	2.0	1.3	1.2	1.9	1.5
Ceshui	Douling(DL)	0.8	3.6	2.4	1.4	2.0	1.8
	avg.	0.9	5.0	2.3	1.4	2.2	1.8

Table 2. Results of TOC, Ro and XRD mineralogy for some representative shale samples

ID	Formation	samples	Lithofacies	TOC (%)	Ro (%)	quartz (%)	feldspar (%)	carbonate (%)	pyrite (%)	clay (%)
1	Dalong	QXJ02	Calcareous shale	0.6	1.7	39.1	0.0	35.2	0.0	25.7
2	Dalong	QXJ05	Calcareous shale	4.6	1.2	50.6	0.0	30.0	1.3	18.1
3	Dalong	QXJ08	black siliceous shale	3.2	1.2	86.2	2.8	0.0	0.0	11.0
4	Dalong	DPQ02	Calcareous shale	0.9	2.0	52.6	4.6	32.7	0.0	10.1
5	Dalong	DPQ03	black shale	5.9	1.8	43.8	12.5	1.6	0.0	42.1
6	Dalong	DPQ06	black shale	6.1	1.5	79.3	4.4	0.0	4.3	12
7	Dalong	DQ09	black shale	6.3	1.3	53.8	1.4	0.0	13.1	31.7
8	Longtan	DLS02	black carbonaceous shale	8.8	1.4	47.6	14.2	0.0	13.1	25.1
9	Longtan	DLS05	black carbonaceous shale	6.9	1.5	48.9	4.3	0.0	8.9	37.9
10	Longtan	NT02	black shale	3.2	1.6	64.6	0.0	0.0	0.0	35.4
11	Longtan	NT03	black shale	3.1	1.5	70.3	0.0	0.0	0.0	29.7
12	Longtan	QXJ10	black carbonaceous shale	8.2	1.8	50.8	0.0	0.0	9.2	40.0
13	Longtan	QXJ14	black shale	3.5	1.4	50.0	2.4	0.0	1.0	46.6
14	Ceshui	XD01	dark-grey shale	1.5	1.8	53.7	0.0	0.0	0.0	46.3
15	Ceshui	XD06	dark-grey shale	0.4	1.7	62.9	0.5	1.1	0.0	35.5
16	Ceshui	JZS05	dark-grey shale	1.4	2.4	60.4	0.0	0.0	0.0	39.6
17	Ceshui	JZS07	dark-grey shale	1.3	1.6	54.4	0.0	0.0	0.0	45.6
18	Ceshui	JZS09	black carbonaceous shale	6.1	1.7	29.2	0.0	1.7	0.0	69.1
19	Ceshui	LMJ02	dark-grey shale	1.2	1.6	52.2	0.0	0.0	0.0	47.8
20	Ceshui	LMJ06	silty shale	0.7	1.7	39.0	0.0	0.0	3.7	57.3
21	Ceshui	ZY04	black shale	2.3	2.0	50.9	0.0	0.7	8.6	39.8
22	Ceshui	ZY08	Calcareous shale	2.2	2.1	19.3	0.0	48.2	4.8	27.7
23	Ceshui	LSJ01	black carbonaceous shale	10.7	2.0	63.7	0.0	0.0	0.0	36.3
24	Ceshui	LSJ04	black carbonaceous shale	7.4	2.1	60.0	0.0	0.0	0.0	40.0
25	Ceshui	LSJ05	dark-grey shale	0.4	2.4	61.5	0.0	0.0	0.0	38.5

Table 3. Rock Density, Porosity, and Permeability for Carboniferous–Permian shale in central Hunan

ID	Formation	samples	TOC (%)	Rock density (g/cm ³)	Porosity (%)	Permeability (mD)
1	Dalong	QXJ02	0.6	2.60	0.5	0.0032
2	Dalong	QXJ05	4.6	2.53	5.2	0.0040
4	Dalong	DPQ02	0.9	2.51	4.2	0.0031
5	Dalong	DPQ03	5.9	2.62	5.1	0.0072
6	Dalong	DPQ06	6.1	1.49	12.0	0.0470
7	Dalong	DPQ09	6.3	2.40	6.9	0.0026
8	Longtan	DLS02	8.8	1.66	14.0	0.0067
9	Longtan	DLS05	6.9	1.78	8.2	0.0089
10	Longtan	NT02	3.2	1.45	5.6	0.0034
11	Longtan	NT03	3.1	1.46	9.2	0.0250
15	Ceshui	XD06	0.4	2.60	1.4	0.0045
16	Ceshui	JZS05	1.4	2.57	2.3	0.0034
22	Ceshui	ZY08	2.2	2.53	4.7	0.0046
24	Ceshui	LSJ04	7.4	2.06	8.6	0.0640
25	Ceshui	LSJ05	0.4	2.06	8.0	0.0110

Table 4. Comparison of the shale gas reservoir rocks in central Hunan with other worldwide shale gas source rocks. Setting = depositional environment of source rocks; TOC – Total Organic Carbon; Kerogen = Kerogen Type; Ro = Vitrinite reflectance values; GAC = Gas adsorption capacity. Data for Ceshui, Dalong and Longtan shales from this paper; sources for other data from the study by Dong et al.(2016).

Shale unit	Ceshui shale (China)	Dalong Shale (China)	Longtan Shale (China)	Wufeng-Longmaxi Shale(China)	Haynesville Shale (US)	Woodford shale (US)	Barnett Shale (US)
Age	Carboniferous	Permian	Permian	Ordovician-Silurian	Jurassic	Devonian	Carboniferous
Setting	Transitional	Transitional	Transitional	Marine	Marine	Marine	Marine
TOC (%)	0.4–9.0 (\bar{x} =2.3)	0.4–6.6 (\bar{x} =3.2)	0.8–9.2 (\bar{x} =5.2)	0.4–25.7 (\bar{x} =2.6)	3.0	5.3	3.7
Kerogen	III	II	II	I – II	I – II ₁	I – II ₁	II ₁
Ro (%)	1.8–2.8 (\bar{x} =1.8)	1.1–1.8 (\bar{x} =1.4)	1.1–1.9 (\bar{x} =1.5)	1.6–3.6	1.5	1.5	1.6
Brittle minerals (%)	30.9–67.5 (\bar{x} =55.0)	55.2–89.9 (\bar{x} =75.8)	50.8–70.3 (\bar{x} =58.9)	21.0–44.0	35.0–65.0	50.0–75.0	40.0–60.0
Porosity (%)	1.4–8.6 (\bar{x} =5.0)	0.5–12.0 (\bar{x} =5.7)	5.6–14.0 (\bar{x} =9.3)	5.2	8.3	5.0	5.0
Permeability (mD)	0.003–0.064 (\bar{x} =0.018)	0.003–0.047 (\bar{x} =0.011)	0.003–0.025 (\bar{x} =0.011)	0.221	0.350	0.050	0.050

Figures

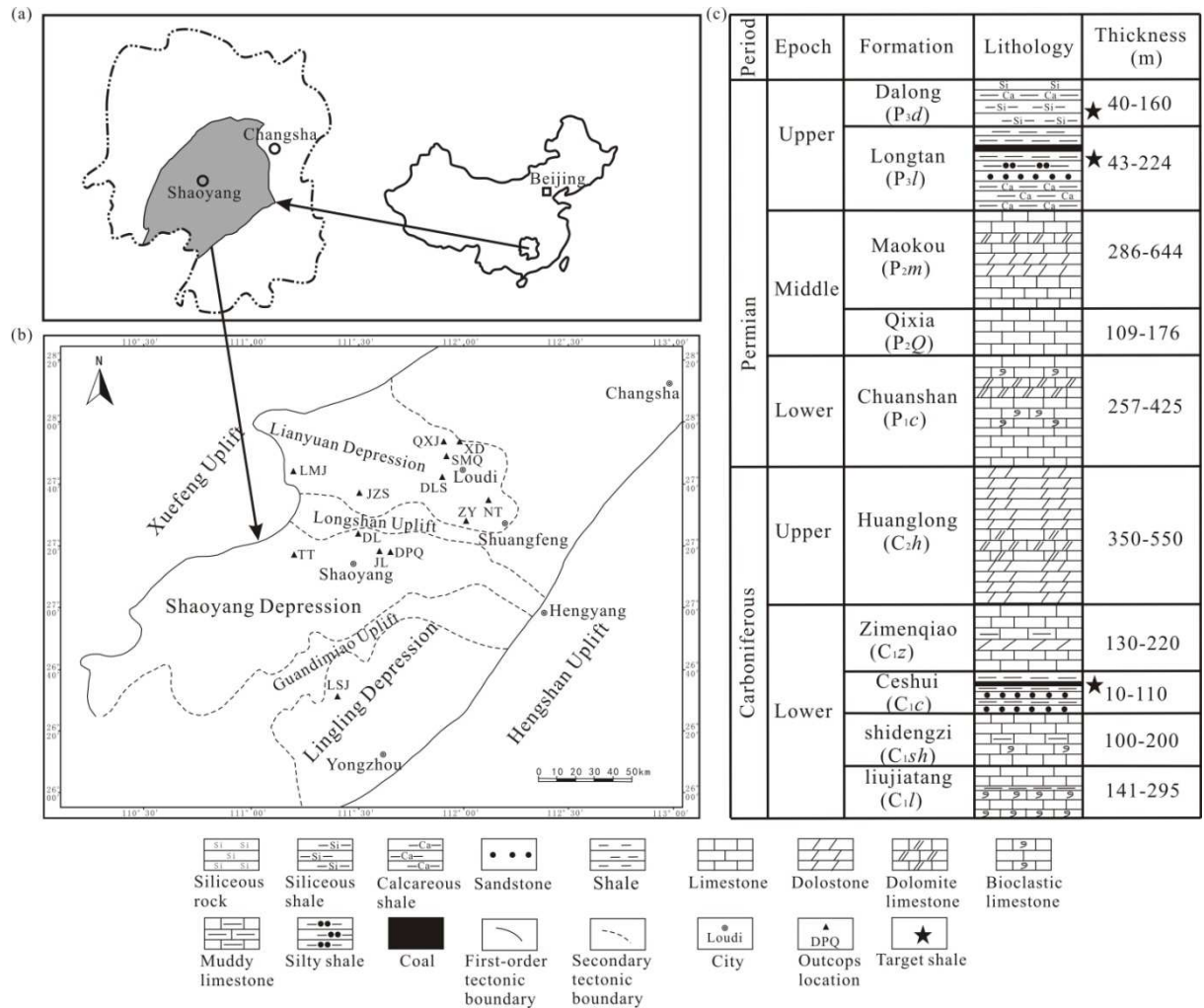


Figure1 (a) The position of Hunan Province and study area; (b) Regional geological map and sampling locations; (c) Generalized stratigraphic column of Permo-Carboniferous strata of the study area (Modified after Jing et al., 2013).

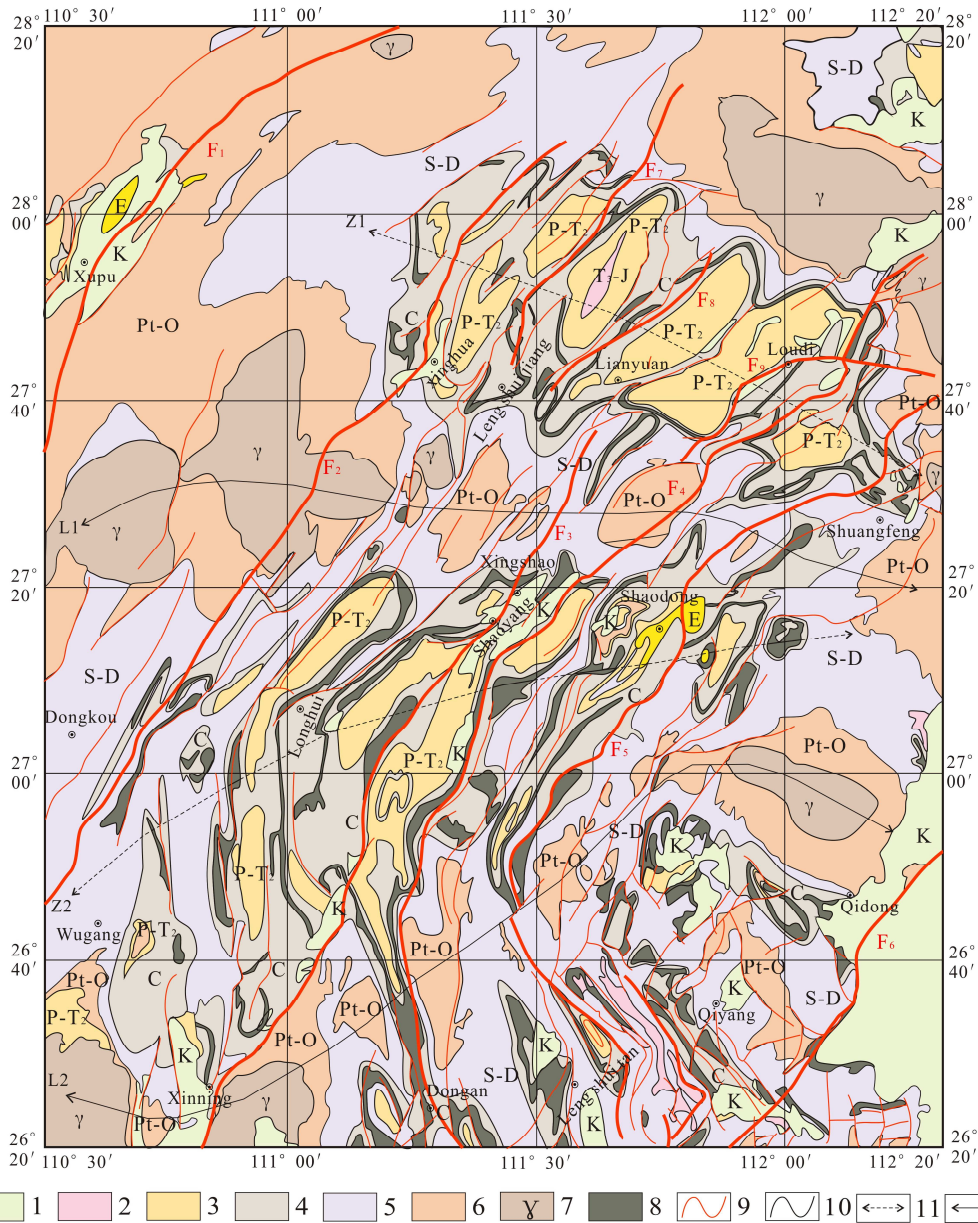


Figure 2 Structure geology map of the central Hunan (Modified from Li et al. 2013). 1. Cretaceous; 2. Upper Triassic-Jurassic; 3. Permian-Middle Triassic; 4. Carboniferous; 5. Silurian-Devonian; 6. Proterozoic-Ordovician; 7. Magmatic body; 8. Coal measures; 9. Fault line; 10. Stratigraphic boundary; 11. Depression; 12. Uplift; F1. Anhua-Xupu fault; F2. Chengbu-Xinhua fault; F3. Xinshao-Xinning fault; F4. Miluo-Shaoyang fault; F5. Qiyang Arc fault; F6. Zhuzhou-Shuangpai fault; F7. Jiyun fault; F8. Jinpanlun fault; F9. Fengguanshan fault; Z1. Lianyuan Depression; Z2. Shaoyang Depression; L1. Baimashan-Longshan bead-shape uplift; L2. Niuxingzhai-guandimiao bead-shape uplift.

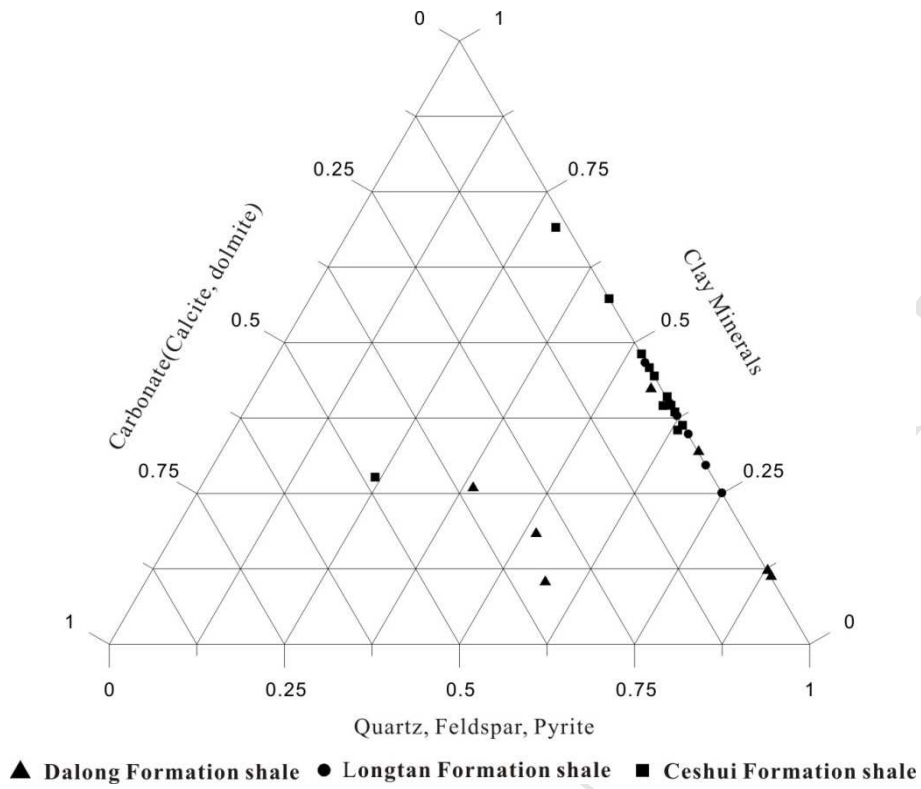


Figure 3. Ternary diagram of mineralogical constituents

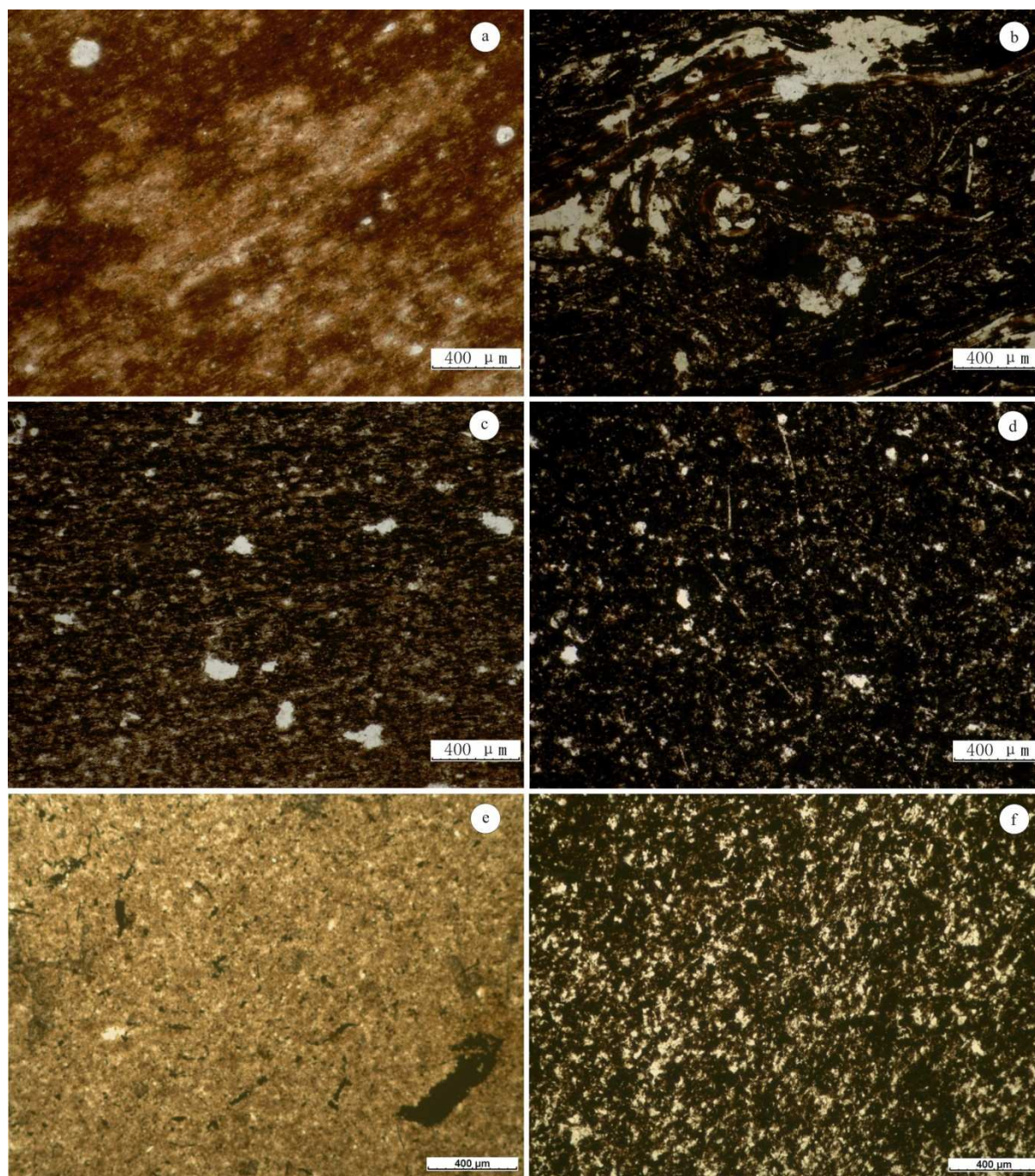


Figure 4. Micro-photographic images of Carboniferous-Permian shale samples. (a) Upper Permian Dalong calcareous shale (QXJ05) from the Qixingjie section. Quartz and carbonate concentrate in the white laminae, while clay and organic matter concentrate in the black laminae. (b) Upper Permian Dalong nonlaminated shale (DPQ06) from the Duanpoqiao section. The dark area is mainly composed of organic matter and clay, while the light area primarily comprises quartz and feldspar. (c) Upper Permian Longtan nonlaminated shale (NT02) from the Nantang section. The dark area consists of organic matter and clay, and the light is mainly quartz. (d) Upper Permian Longtan carbonaceous shale (DLS05) from the Doulishan section. The dark area is mainly organic matter and clay, and the light is mainly quartz and feldspar. (e) Lower Carboniferous Ceshui silty shale (LMJ06) from the

Lumaojiang section. Clay minerals occupy a large area in the texture, while organic matter and quartz scatter in the matrix. (f) Lower Carboniferous Ceshui carbonaceous shale (LSJ04) from the Liangshuijing section. The dark place is mainly organic matter and the light is mainly quartz. Organic matter aggregates or particles are randomly distributed in the matrix.

ACCEPTED MANUSCRIPT

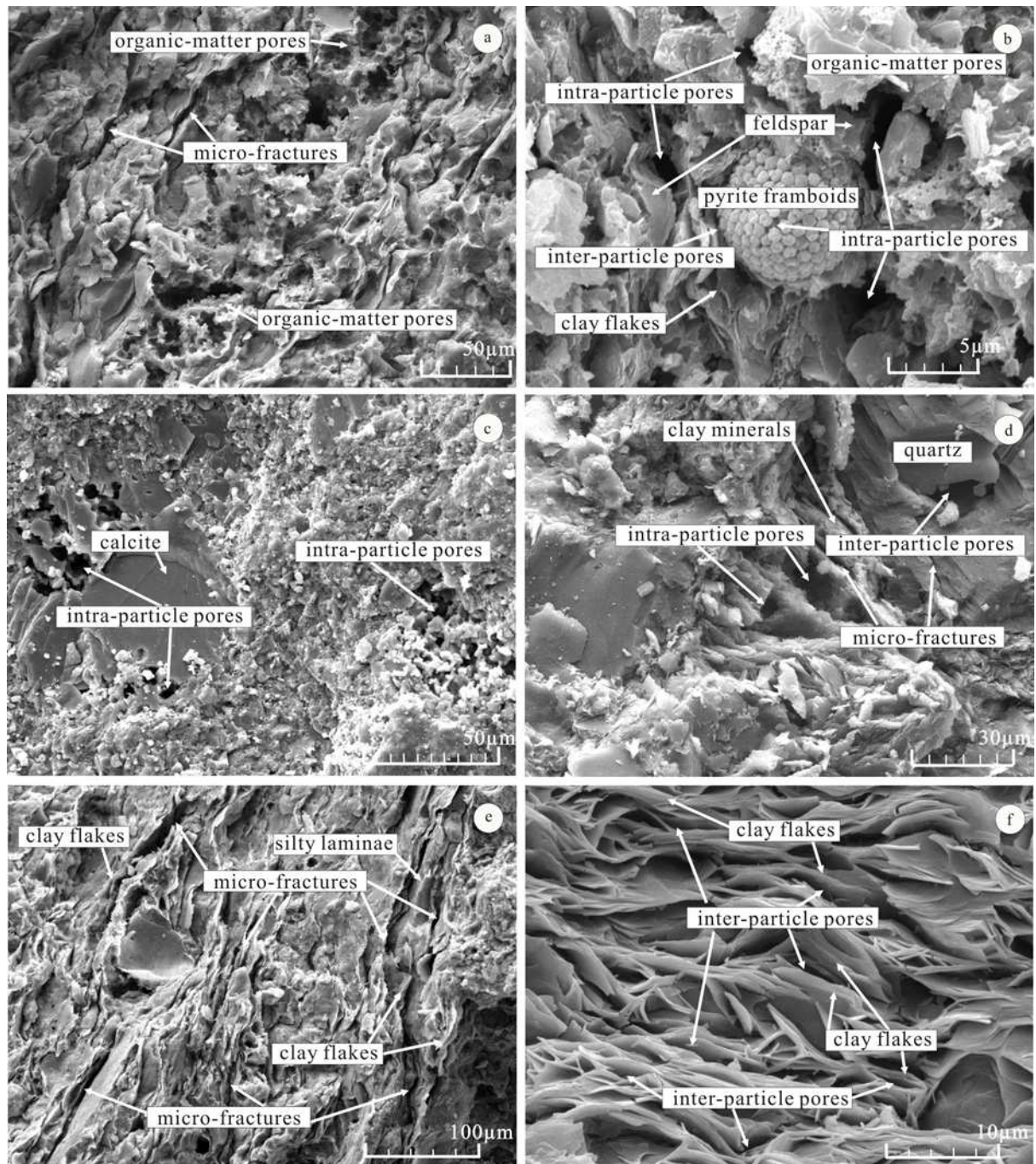


Figure 5. SEM images of Carboniferous–Permian shale samples. (a) Lower Carboniferous Ceshui carbonaceous shale (LSJ04) from the Liangshuijing section. “Honeycomb” organic pores and micro-fractures are well developed. (b) Upper Permian Longtan carbonaceous shale (DLS05) from the Doulishan section. Intra-particle pores exist in the pyrite framboids and the feldspar minerals. Inter-particle pores between pyrite crystals and clay flakes, and “honeycomb” organic–matter pores generated by hydrocarbon expulsion are well developed. (c) Upper Permian Dalong calcareous shale (QXJ02) from the Qixingjie section. Intra-particle pores in the carbonate minerals are well developed. (d) Upper Permian Dalong shale (DPQ03) from the Duanpoqiao section. Inter-particle pores occur between quartz minerals, intra-particle pores exist in the feldspar minerals and micro-fractures in clay

minerals and at weak interfaces are well developed. (e) Lower Carboniferous Ceshui carbonaceous shale (LSJ05) from the Liangshuijing section. Micro-fractures between clay flakes or between clay laminae and silty laminae are well developed. (f) Lower Carboniferous Ceshui silty shale (LMJ06) from the Lumaojiang section. Inter-particle pores in the clay flakes are well developed.

ACCEPTED MANUSCRIPT

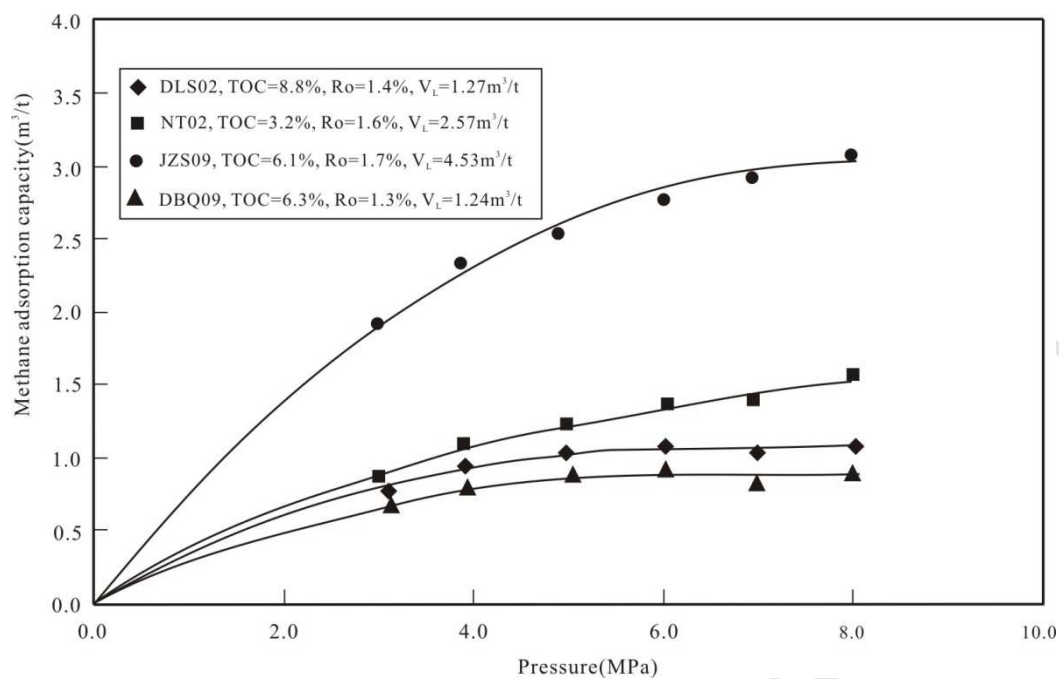


Figure 6. Methane adsorption isotherms at 40 °C

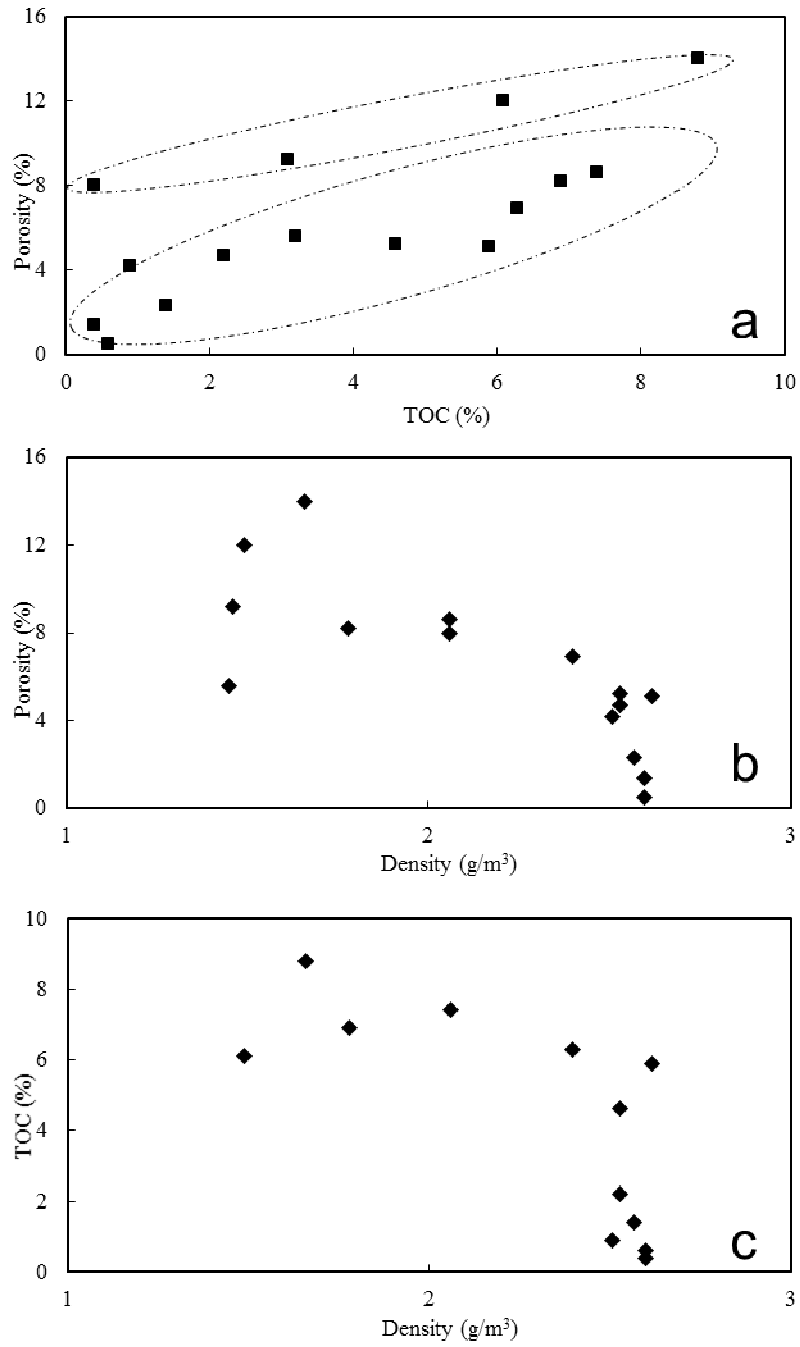


Figure 7. Correlation plots of porosity with (a) TOC content, (b) density, and (c) TOC content with density for Permo-Carboniferous shale samples in Central Hunan Province.

- Methane adsorption capacity is between 1.24 cm³/g and 4.53 cm³/g.
- Mean porosity and permeability are 6.4% and 0.013md, respectively.
- Carboniferous and Permian shales are abundant in type III and II organics, respectively.
- Thermal maturity is locating in the wet gas window.
- Mineral constituents are dominated by brittle minerals.

ACCEPTED MANUSCRIPT